This is an open access article published under an ACS AuthorChoice License, which permits copying and redistribution of the article or any adaptations for non-commercial purposes.

THE JOURNAL OF PHYSICAL CHEMISTRY C

Article

pubs.acs.org/JPCC

Photoelectrochemistry by Design: Tailoring the Nanoscale Structure of Pt/NiO Composites Leads to Enhanced Photoelectrochemical Hydrogen Evolution Performance

András Sápi,[†] András Varga,[‡,§] Gergely F. Samu,[‡,§] Dorina Dobó,[†] Koppány L. Juhász,[†] Bettina Takács,[‡,§] Erika Varga,[§] Ákos Kukovecz,[†,⊥] Zoltán Kónya,[†,∥] and Csaba Janáky*[,‡,§]

[†]Department of Applied and Environmental Chemistry, University of Szeged, Rerrich Square 1, Szeged, H-6720, Hungary
[‡]MTA-SZTE "Lendület" Photoelectrochemistry Research Group, University of Szeged, Rerrich Square 1, Szeged, H-6720, Hungary
[§]Department of Physical Chemistry and Materials Science, University of Szeged, Rerrich Square 1, Szeged, H-6720, Hungary
[⊥]MTA-SZTE "Lendület" Porous Nanocomposites Research Group, University of Szeged, Rerrich Square 1, Szeged, H-6720, Hungary
[∥]MTA-SZTE Reaction Kinetics and Surface Chemistry Research Group, University of Szeged, Rerrich Square 1, Szeged H-6720, Hungary

Supporting Information

ABSTRACT: Photoelectrochemical hydrogen evolution is a promising avenue to store the energy of sunlight in the form of chemical bonds. The recent rapid development of new synthetic approaches enables the nanoscale engineering of semiconductor photoelectrodes, thus tailoring their physicochemical properties toward efficient H_2 formation. In this work, we carried out the parallel optimization of the morphological features of the semiconductor light absorber (NiO) and the cocatalyst (Pt). While nanoporous NiO films were obtained by electrochemical anodization, the monodisperse Pt nanoparticles were synthesized using wet chemical methods. The Pt/NiO nanocomposites were characterized by XRD, XPS, SEM, ED, TEM, cyclic voltammetry, photovoltammetry, EIS, etc. The relative enhancement of the photocurrent was demonstrated as a function of the nanoparticle size and loading. For mass-specific surface activity the smallest nanoparticles (2.0 and 4.8 nm) showed the best performance. After deconvoluting the trivial geometrical effects (stemming from the variation of Pt particle size and thus the electroactive surface area), however, the intermediate particle sizes (4.8 and 7.2 nm) were found to be optimal. Under optimized conditions, a 20-fold increase in the photocurrent (and thus the H_2 evolution rates) was observed for the nanostructured Pt/NiO composite, compared to the benchmark nanoparticulate NiO film.

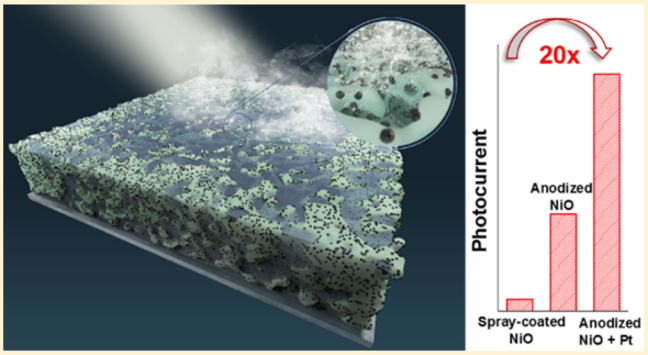

INTRODUCTION

With rapidly increasing global renewable energy harvesting capacities there is a rising interest for energy storage solutions, to overcome the intermittent nature of the various renewable energy sources. Photoelectrochemical (PEC) H_2 evolution reaction (HER) and CO_2 conversion are both promising avenues to generate solar fuels and thus store the energy of sunlight in the form of chemical bonds.[1,2] One of such PEC procedures is the direct reduction of H^+ ions at the interface of a p-type semiconductor (SC) photocathode and a liquid electrolyte. Alternatively, when irradiating an n-type SC, water oxidation occurs at the SC/electrolyte interface, while HER can proceed on the counterelectrode. A range of photocathodes has been screened during the past decades,[3−6] and reasonable solar to hydrogen conversion efficiencies have been achieved employing complex electrode assemblies.[7,8] At the same time, there are still several open questions to be answered before high activity, stability, and selectivity could be achieved at the same time.[9]

Recent studies indicated that the use of nanostructured photoelectrodes may help to enhance electron transfer rates to levels which make practical significance.[10,11] While the high specific area (i.e., roughness factor) is a key advantage in electrocatalysis, the picture is much murkier in the photoelectrocatalytic scenario, because nanostructuring of photoelectrodes has both benefits and drawbacks. For example, charge carrier recombination due to both surface traps and the necessity of hopping from one particle to another, certainly decreases the achievable solar to chemical conversion efficiencies. Interconnected nanostructures may help to circum-

Received: January 16, 2017
Revised: April 4, 2017
Published: April 5, 2017

© 2017 American Chemical Society

DOI: 10.1021/acs.jpcc.7b00429
J. Phys. Chem. C 2017, 121, 12148−12158

vent this issue, by eliminating the need of interparticle charge transfer. Different examples can be cited, ranging from mesoporous TiO_2 vs TiO_2 nanotubes,[12,13] nanoparticulate and nanoporous WO_3,[14,15] and so forth.

NiO has been increasingly studied as a photocathode material, recently. NiO may also have practical significance in p-type DSSCs, in an inverted configuration compared to its TiO_2-based counterpart.[16−18] Interestingly, although the NiO is long known to be capable of both evolving H_2 and reducing CO_2 (based on its conduction band edge position),[19] its solar fuel generation ability has not been extensively studied. There are a few examples, where NiO was studied in conjunction with either a solid state or molecular cocatalyst, in HER and CO_2 ER. For example, a NiO/Cu_2O heterojunction was employed as both light absorber and H_2-evolution catalyst.[20] In another study, NiO was decorated with a Ru-dye and Ni catalyst to achieve visible light driven PEC H_2-evolution.[21] PEC CO_2 conversion to CO was demonstrated in combination with a Ru(II)−Re(I) containing supramolecular catalyst.[22] With respect to morphological questions, the PEC behavior of a nanoparticulate NiO film was compared with compact NiO recently, with special focus on their characterization with surface photovoltage spectroscopy.[23] On the other hand, there is only one single report on the PEC properties of interconnected NiO nanostructures.[24] The versatility of NiO is reflected in the fact that it has been also studied as protective coating for Si photoanodes, in solar fuel generation processes.[25,26]

Combination of a SC light absorber with a metal electrocatalyst is a promising avenue to further enhance the solar to chemical conversion efficiency, because the light absorption and charge transfer is decoupled. Consequently, by intimately linking an electrocatalyst to the SC surface a Schottky-junction can be formed, which in turn facilitates the rapid charge carrier extraction from the SC to the metal cocatalyst.[27,28] PEC H_2-evolution takes place in the next step, on the surface of the metal nanoparticle cocatalyst. While various cocatalysts have been examined,[29] Pt is still considered as the state-of-the-art electrocatalyst for the EC HER.

The effect of Pt size was studied in different electrocatalytic processes. For example, in oxygen reduction reaction (ORR) the mass specific activity was increased sharply in the range of 1.2−2.2 nm Pt particles and slightly decreased for even larger particle sizes (>2.5 nm).[30] In another study CO electrooxidation was studied on Pt nanoparticles ranging from 1 to 30 nm, and the importance of particle shape and specific adsorption was also highlighted.[31] Similarly, Pt has been heavily studied and utilized as (co)catalyst in both thermally- and photoactivated heterogeneous catalysis. The effect of Pt nanoparticle size (diameter of 1−10 nm) on their heterogeneous catalytic activity was studied for both gas and liquid phase reactions. For example, in the case of alcohol oxidation, larger particles had higher activity towards the formation of aldehydes, ketones, and carbon-dioxide.[32−34] For benzene and toluene hydrogenation, ∼ 2−3 nm sized Pt nanoparticles had outstanding activity compared to both smaller and larger nanoparticles.[35] In photocatalytic hydrogen evolution (using oxalic acid as sacrificial e^- donor) over TiO_2 supported Pt nanoparticles, 3 nm sized particles showed the best activity compared to both smaller and bigger particles.[36] Photodriven CO_2 reduction was performed on Pt/TiO_2 composites, containing photodeposited ultrasmall Pt nanoparticles (below 2 nm).[37] The particle size and density on the PEC performance was also studied for Pt/Si samples, involving relatively large Pt particles (40−300 nm) on flat Si electrodes.[38]

Taking all the above listed precedencies as a whole, it is clear that there is considerable scope for the nanoscale engineering of both the light absorber and the cocatalyst in metal/SC composite electrodes. In this paper we report on high PEC H_2 generation rates on optimized Pt/NiO nanostructures. We studied the effect of the NiO nanostructure as well as the Pt cocatalyst size (and loading), where we found that there is an optimal particle size and loading. Under properly adjusted conditions, a 20-fold increase in the photocurrent (and thus the H_2 evolution rates) was observed compared to the benchmark nanoparticulate NiO film. Finally, we verified that particle size of the cocatalyst in a PEC configuration is equally important as it was in the previously studied electrocatalytic and photocatalytic scenarios.[30−35]

EXPERIMENTAL SECTION

Materials. For the anodization experiments Ni foils (99.9+ %, 0.125 mm thick), NH_4F (≥99%), and ethylene glycol (≥99%) were all purchased from Sigma-Aldrich, and KOH (≥86% in water) was obtained from Fluka. For cleaning the metal foils ethanol (Chromanorm) 2-propanol (Chromanorm), and acetone (Rectapur) were purchased from VWR. For the electrochemical measurements Na_2SO_4 (99%, Alfa Aesar) was used, along with N_2 gas (99.995%, Messer, Budapest, Hungary). All solutions were prepared with ultrapure water (Milli-Q, ρ = 18.2 MΩ cm). All chemical reagents were used without further purification.

Anodization of the Ni Foil. Prior to anodization, the Ni foils were mechanically polished to mirror finish using silicon carbide sandpaper with successively finer roughness. To ensure the removal of any attached organic contaminants three subsequent steps (5 min) of ultrasonication in acetone, 2-propanol, and finally ultrapure water were performed. The anodization was carried out in a standard two-electrode setup, where the Ni foil acted as the anode and a Pt foil as the cathode. The Ni foil was pressed between two O-rings, leaving 2.27 cm^2 exposed to the electrolyte, while the electric contact was located on the back of the sample. The anodization was carried out at different voltages using a programmable DC power supply (Voltcraft PSP 1803), while the procedure was monitored by a digital multimeter (Keithley 2000). Both instruments were controlled by custom-written LabVIEW software. Immediately after the anodization, the samples were carefully washed with ultrapure water and dried in N_2 stream. To obtain the desired crystalline phase of NiO, the anodized samples were annealed for 4 h at 500 °C, with a heating ramp of 10 °C min^{-1} (Thermo Scientific Heraeus K114 Furnace).

Three different electrolyte compositions were used (the first two were adopted from the literature)[24,39] to perform the anodization:

(i) Aqueous solution consisting of 0.5 M NH_4F dissolved in 85 wt % H_3PO_4, with an anodization voltage of 6 V − 10 V, for 10 min.[39]
(ii) Organic media consisting of 0.5 wt % KOH, 5 wt % H_2O, and 94,5 wt % ethylene glycol with an anodization voltage of 40 − 60 V and duration of 1 h.[24]
(iii) A combined electrolyte consisting of an ethylene glycol solution containing 0.15 M KOH, 0.1 M NH_4F, and 3% v/v of H_2O. During these syntheses the voltage was held at 30 V for 1 h.

DOI: 10.1021/acs.jpcc.7b00429
J. Phys. Chem. C 2017, 121, 12148−12158

Preparation of Pt Nanoparticles. Pt nanoparticles with various sizes were synthesized as described in the Supporting Information.[34] Briefly, NaOH and polyvinylpyrrolidone (M_w = 29 000) were dissolved in ethylene glycol together with the platinum precursor ($H_2PtCl_6{\cdot}xH_2O$ or platinum(II) acetylacetonate). Subsequently, the mixture was heated to 160−200 °C in an oil bath and held at that temperature between 10 min and 2 h under argon atmosphere. Pt nanoparticles in five different sizes were synthesized, with a diameter of 2.0 ± 0.4, 4.8 ± 0.7, 7.2 ± 0.8, 8.6 ± 1.3, and 12.3 ± 1.4 nm. The resulting Pt nanoparticles were precipitated with acetone, centrifuged and dispersed in ethanol. Finally, the nanoparticles were repeatedly washed with hexane, centrifuged, and redispersed in ethanol before use. The exact concentration of the Pt suspensions was determined by ICP-MS measurements (Agilent 7700x type ICP-MS spectrometer).

Drop-Casting of Pt on the NiO Films. First the NiO samples were cut into four pieces with equivalent geometric areas of 0.57 cm^2 to minimize the possible error arising from the use of different samples. One piece was always kept as an internal reference and every normalization was carried out with respect to this. The suspension of different sized Pt nanoparticles was prepared in ethanol (sonicated for 60 min) and was then drop-casted on the surface of the NiO samples (preheated on a hot plate at 65 °C). Investigations were carried out with different Pt loadings (0.5−4.0 $\mu g\ cm^{-2}$). To improve the adherence between the Pt nanoparticles and the NiO scaffold, and to remove the capping polyvinylpyrrolidone from the Pt surface, the as prepared Pt/NiO composites were annealed in air at 300 °C for 2 h with a heating ramp of 5 °C min^{-1}.

Physical Characterization. The X-ray diffraction (XRD) patterns were recorded with a Rigaku MiniFlex II benchtop instrument with Cu Kα X-ray source (λ = 1.5406 Å), in the 20−80° range, with a 2° min^{-1} scan rate. Raman spectra were recorded with a Thermo Scientific DXR Raman microscope at an excitation wavelength of 532 nm, applying 10 mW laser power, and averaging 20 spectra with an exposition time of 6 s. Scanning electron microscopic (SEM) images were captured using a Hitachi S4700 FE-SEM instrument. Transmission electron microscopic (TEM) investigation and electron diffraction analysis were performed using a FEI Tecnai G^2 20 X-Twin type instrument, operating at an acceleration voltage of 200 kV. The Pt containing ethanol based suspensions were drop-casted on carbon film coated copper grids. In the case of the NiO samples, a small part of the surface of the electrode materials was scratched into a tiny jar filled with ethanol before ultrasonication. X-ray photoelectron spectra were recorded with a SPECS instrument equipped with a PHOIBOS 150 MCD 9 hemispherical analyzer. The analyzer was operated in the fixed analyzer transmission (FAT) mode with 20 eV pass energy. The Al K_α radiation ($h\nu$ = 1486.6 eV) of a dual anode X-ray gun was used as an excitation source. The gun was operated at 210 W power (14 kV, 15 mA). The binding energy scale was corrected by fixing the main C 1s component to 285.0 eV, corresponding to the adventitious carbon. For spectrum acquisition and evaluation both manufacturers (SpecsLab2) and commercial (CasaXPS, Origin) software packages were used.

Electrochemical Measurements. All electrochemical measurements were performed using an Autolab PGSTAT302N instrument equipped with an FRA32 M module. The measurements were carried out in a standard three electrode setup, where the studied Pt/NiO acted as working electrode, a platinum foil and Ag/AgCl (saturated NaCl) electrode were used as the counter and the reference electrodes, respectively. The electrolyte was purged with N_2 gas for 20 min before each measurement.

Photoelectrochemical measurements were carried out in a sealed two compartment, quartz cell where 0.1 M Na_2SO_4 solution was used as the electrolyte. Linear sweep voltammograms were recorded from 0.0 to −1.0 V with a sweep rate of 2 mV s^{-1} under periodically chopped illumination (0.1 Hz). The light source was a 300 W Hg−Xe arc lamp (Hamamatsu L8251). The radiation source was placed 3 cm away from the working electrode surface. During the long-term PEC measurements, the potential was held at E = −0.8 V, the solution was stirred continuously, and the solution temperature was kept constant at 25 °C. In these experiments, the gas phase products were detected with a gas chromatograph (Shimadzu GC-2010 Plus equipped with a barrier ionization discharge (BID) detector).

For the electrochemical impedance spectroscopy (EIS) measurements a closed electrochemical cell was employed, where 1.0 M Na_2SO_4 solution was used as the electrolyte. Prior to each EIS measurement, five cyclic voltammetry (CV) scans were recorded in the range of −0.8 to 1.0 V with a 50 mV s^{-1} sweep rate to ensure proper wetting of the porous electrodes and to estimate the electroactive surface area of the Pt nanoparticles. All impedance spectra were recorded at two different potential values (E = 0.0 V and E = −0.6 V), in the 10 Hz to 0.1 MHz frequency range, using a sinusoidal excitation signal (10 mV RMS amplitude).

Incident photon-to-electron conversion efficiency (IPCE) measurements were performed on a Newport Quantum Efficiency Measurement System (QEPVSI-B) in a single-compartment, three electrode quartz electrochemical cell. The wavelength range was 250−400 nm ($\Delta\lambda$ = 10 nm step size). The IPCE profiles were recorded in a 0.2 M Na_2SO_4 solution at E = −0.8 V bias potential.

RESULTS AND DISCUSSION

Anodization of Ni Foils. As described in the Experimental Section, anodization of Ni foils was carried out in three different complexing agent containing media. The first method employed F^- ions, dissolved in concentrated H_3PO_4 media.[39] Different anodization voltages were used, and by increasing the applied voltage, the gradual increase of the steady-state current was observed (Figure S1). This trend is related to the rate of the dissolution of the metal-oxide layer,[24] and also affects the pore size of the obtained porous electrodes.[40] The samples prepared at 6 V showed a compact morphology, whereas the presence of nanopores was observed at higher anodization voltages (see SEM images in Figure S2). Unfortunately, this method led to F and P-impurities in the structure (see further discussion and EDX data in Figure S3A), which deleteriously affected the PEC response of the prepared electrodes (Figure S3B). To prevent the incorporation of the phosphate impurity, our attention shifted to a method employing a glycerol based media with KOH as the complexing agent.[24] In this case, however, a high etching rate of the formed NiO layer was observed (hindering morphology control), which eventually leads to the complete dissolution of the Ni foils. To combat both the phosphate inclusion and the fast dissolution of the formed NiO, a complex media was employed. The optimized synthesis media consisted of ethylene glycol as the solvent,

DOI: 10.1021/acs.jpcc.7b00429
J. Phys. Chem. C 2017, 121, 12148−12158

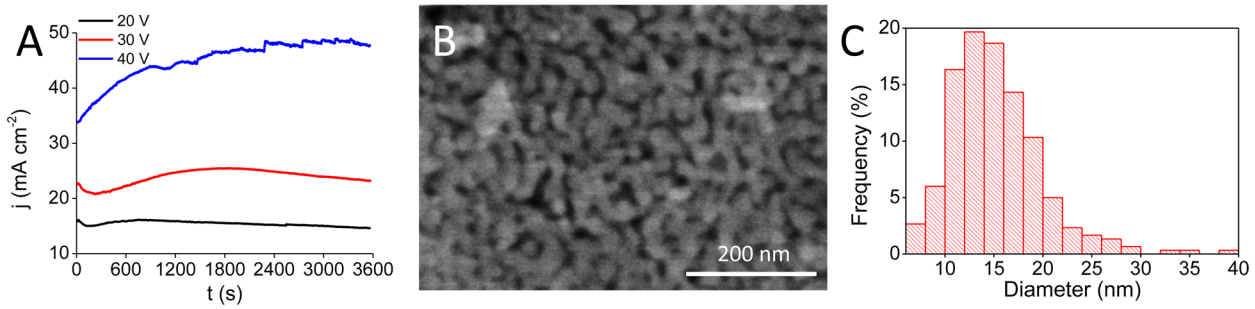

Figure 1. (A) The effect of applied voltage on the anodization traces recorded in 0.15 M KOH, 0.1 M NH_4F, and 3% v/v of H_2O containing ethylene glycol. (B) SEM image of the heat treated (T = 500 °C, 1 h) NiO sample obtained at U = 30 V, 1 h. (C) Pore size distribution of a typical NiO sample (U = 30 V, 1 h) annealed at T = 500 °C for 1 h.

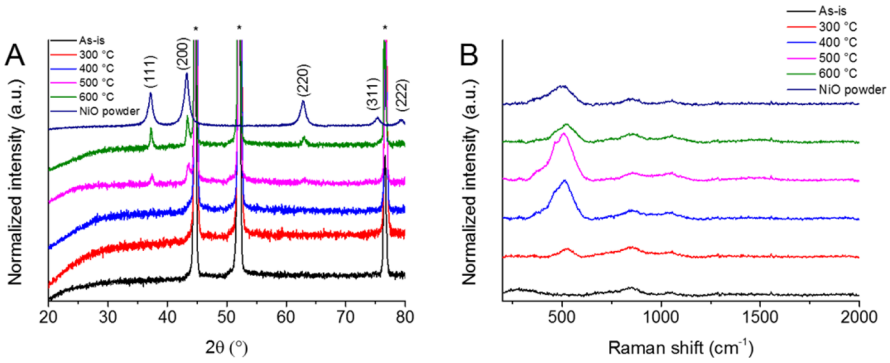

Figure 2. (A) XRD patterns recorded for the anodized NiO samples (U = 30 V, 1 h) heat treated at different temperatures for 1 h and the reference NiO powder. (B) Raman spectra recorded for the nanoporous NiO samples (U = 30 V, 1 h) heat treated at different temperatures and the reference NiO powder.

which contained 0.15 M KOH, 0.1 M NH_4F, and 3% v/v of H_2O.

The use of organic solvent necessitated higher anodization voltages compared to the aqueous synthesis (because of higher solution resistance). As the anodization voltage was increased, faster NiO etching was observed (Figure 1A). Another typical feature of the anodization curves was the appearance of a distinct current density maximum.[41,42] This can be attributed to the increasing electrode surface area caused by the extensive pore formation. When the two competing reactions (oxide formation and dissolution) reach a steady state level, however, near-constant current densities stabilized at the later stages of anodization.

SEM images were recorded to probe the morphology of the NiO films obtained at different anodization voltages. The nanoporous morphology was witnessed for all samples, but the pore size was found to be dependent from the anodization voltage (Figure 1B and Figure S5). On the high magnification SEM image, the interconnected nanoporous structure can be observed (Figure 1B). The size of the obtained pores fall into the range of 15 ± 5 nm (see pore size distribution in Figure 1C), while the grain size was slightly larger (~20 nm, see also TEM images later in Figure 7). These morphological features show close resemblance to the porous NiO electrodes prepared in fluoride containing electrolytes (first method). We note here that in the case of the glycerol-based alkaline method the formation of macroporous structures were reported.[24] In all further experiments the samples prepared at U = 30 V for 1 h anodization time were used.

Electrochemical anodization usually results in the formation of amorphous oxides materials, thus a subsequent heat treatment step is often necessary. To investigate the effect of heat treatment (300−600 °C) on the crystallinity of the samples, XRD measurements were carried out (Figure 2A). XRD profiles of the pristine NiO and a commercial NiO powder were also included as reference. The pristine anodized sample exhibited no reflections attributable to NiO, only sharp reflections of the Ni foil underneath the amorphous layer were observed (marked with an asterisk). By employing a heat treatment above 500 °C, the development of the most intense reflections of NiO (JCPDS #47−1049) was observed. The average size of the crystalline domains was estimated using the Scherrer equation for the most intensive (111) diffraction. A d = 22 nm value was obtained, very similar to the grain size obtained from the SEM images, which in turn confirms that the samples are fairly crystalline.

To further investigate the structural features of the formed NiO layers Raman measurements were carried out (Figure 2B). The reference NiO powder exhibits three distinguishable Raman active vibration modes, which correspond to one-phonon LO modes (at ~513 cm^{-1}), two-phonon TO + LO (at ~851 cm^{-1}) and 2LO (at ~1048 cm^{-1}) modes, respectively. These values are in close agreement with the reported values in the literature.[43] Furthermore, increasing heat treatment temperature, the gradual evolution of the LO mode was observed. While this vibrational mode is missing in the case of the unannealed (as is) sample, it is immediately observable even after a heat treatment at 300 °C. On the basis of the results from XRD and Raman spectroscopic measurements a heat treatment temperature of 500 °C was chosen for future studies. EDX measurements (Figure S4), however detected

DOI: 10.1021/acs.jpcc.7b00429
J. Phys. Chem. C 2017, 121, 12148−12158

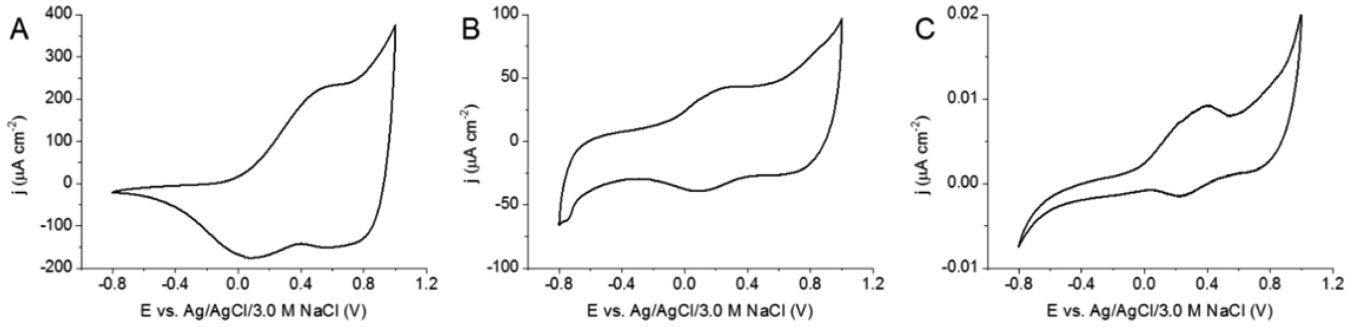

Figure 3. Cyclic voltammograms recorded in 0.2 M Na_2SO_4 with 50 mV s^{-1} sweep rate for (A) nanoporous NiO sample (prepared at U = 30 V, 1 h; heat treated at T = 500 °C, 4 h), (B) NiO powder on glassy carbon electrode, and (C) compact NiO layer (prepared at U = 30 V, no complexing agent, 1 h; heat treated at T = 500 °C, 4 h).

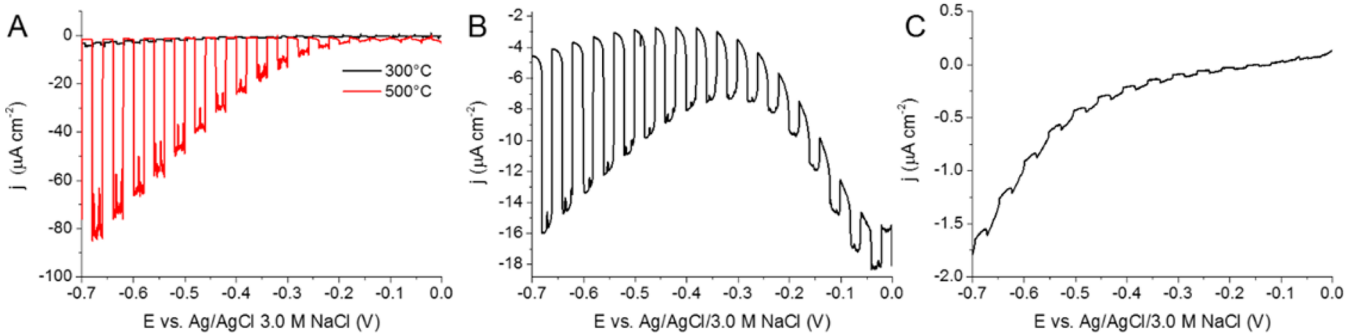

Figure 4. Linear sweep photovoltammograms recorded in 0.2 M Na_2SO_4 with 2 mV s^{-1} sweep rate for (A) nanoporous NiO sample (prepared at U = 30 V, 1 h; heat treated at T = 500 and 300 °C, 4 h), (B) NiO powder on glassy carbon electrode, and (C) compact NiO layer (prepared at U = 30 V, 1 h; heat treated at T = 500 °C, 4 h).

some residual carbon in the samples annealed for 1 h, thus the heat treatment step was extended to 4h.

Electrochemical Measurements. To evaluate the electrochemical behavior of the prepared nanoporous NiO electrodes cyclic voltammograms were recorded (Figure 3A). As reference measurements, NiO powder spray-coated on a glassy carbon electrode (Figure 3B) and a compact NiO layer (Figure 3C) (obtained by replacing the complexing agents in the anodization media with Na_2SO_4) were also studied. NiO usually exhibits two distinct redox peak pairs.[44] The first oxidation peak at E = 0.3 V is attributed to the oxidation of $Ni(OH)_2$ to various NiO(OH) phases eq 1.[44] The exact reaction, however, involves different phases of NiO(OH) as described by the Bode model.[45] The second oxidation peak starting at E> 0.75 V is related to the oxidation of Ni(II) to Ni(III) eq 2.[23]

$$Ni(OH)_2 \rightarrow NiO(OH) + H^+ + e^- \quad (1)$$

$$2NiO + H_2O \rightarrow Ni_2O_3 + 2H^+ + 2e^- \quad (2)$$

In our case, only one broad anodic redox wave was seen centered at $E \sim 0.4$ V, attributed to the redox transformation of $Ni(OH)_2$ to various NiO(OH) phases. By determining the charge capacitance values, it was found that the nanoporous NiO sample surpasses both the spray-coated NiO nanopowder (3-fold increase) and the NiO compact layer (27-fold increase) in term of electroactivity. This enhanced behavior can be mainly attributed to the superior surface area (vs the compact layer) and the interconnected structure (vs nanoparticulate films) of the anodized NiO samples. These observations already projected that the nanoporous NiO films will be a viable platform for future PEC studies.

Photoelectrochemical Measurements. To evaluate the photoresponse of the anodized NiO electrodes linear sweep photovoltammetry measurements were carried out (Figure 4). During illumination, the measured cathodic currents indicated a p-type semiconductor behavior of all studied samples. In these cases, no electron scavenger species was added, thus the photoresponse can be mainly ascribed to the photoreduction of water. Compared to the anodized and heat treated NiO layer (Figure 4A), both the spray-coated NiO nanopowder (Figure 4B) and the compact NiO layer (Figure 4C) showed inferior photoactivity (note the difference in the scale bar of the current density). In the latter two cases this may be the result of inadequate charge carrier extraction. As for the powdered sample, extensive charge carrier recombination may occur on the surfaces of the nanoparticles, which ultimately limits the photoresponse of this material. The case for the compact sample is somewhat different. Although the interfaces between particles are absent, the photogenerated carriers on the surface of the layer cannot be extracted through the bulk of the oxide (note the low conductivity of NiO). Thus, it can be concluded that the anodized sample exhibits superior PEC performance because of its interconnected nanoporous structure.

A further decisive parameter dictating the photoresponse of a material is its crystallinity. In Figure 4A the photoresponse of the anodized NiO samples heat treated at two different temperatures are compared. The sample annealed at 300 °C, which exhibited no crystalline features, showed negligible photocurrents, while the sample heat treated at 500 °C showed $j_{ph} = -80$ μA cm^{-2} at $E = -0.7$ V.

DOI: 10.1021/acs.jpcc.7b00429
J. Phys. Chem. C 2017, 121, 12148−12158

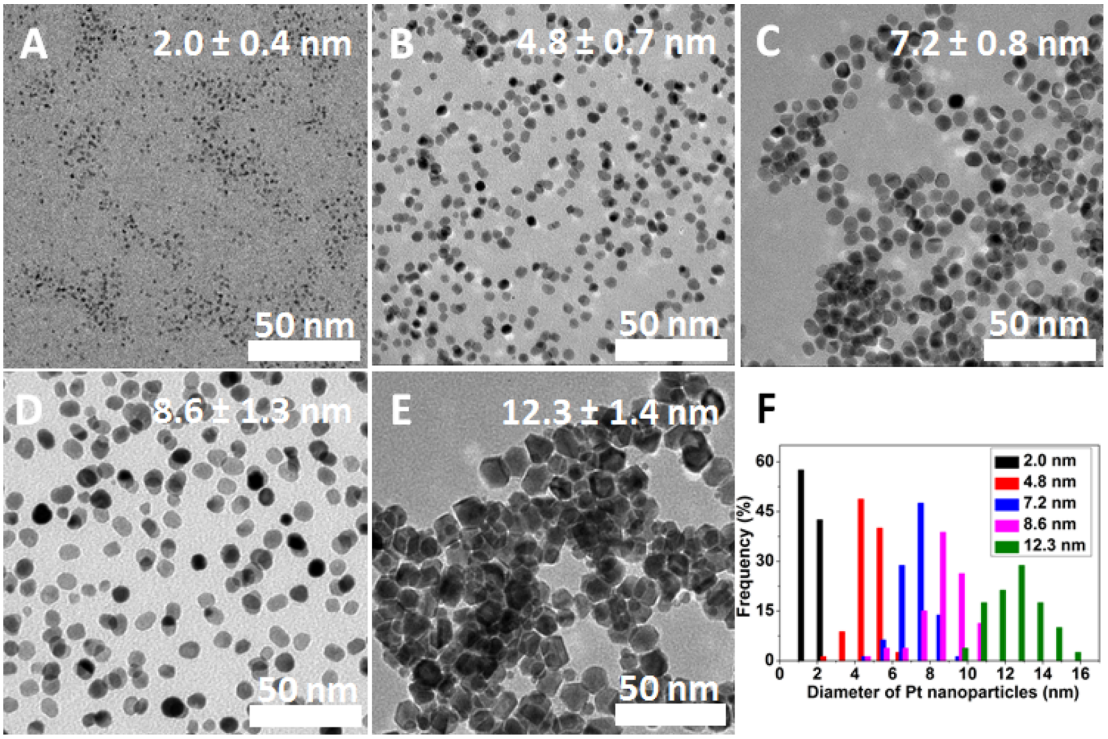

Figure 5. TEM images of the different sized Pt nanoparticles (A–E), together with the comparison of their size distributions (F).

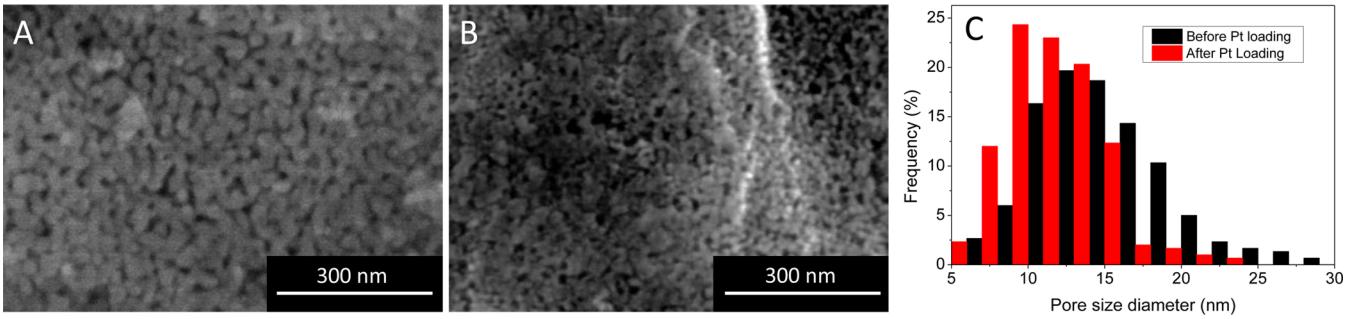

Figure 6. SEM images of (A) an anodized NiO film, (B) a Pt/NiO composite (7.2 nm Pt), and (C) pore size distribution before and after anchoring Pt (determined from SEM images in parts A and B).

Pt Decoration of the NiO Electrodes. Pt nanoparticles with controlled size were synthesized in ethylene glycol by the polyol method using different Pt-based precursors and polyvinylpyrrolidone (PVP) as a capping agent (for more details see Supporting Information). The as-prepared Pt nanoparticles have narrow size distribution with an average diameter of 2.0 ± 0.4, 4.8 ± 0.7, 7.2 ± 0.8, 8.6 ± 1.3, and 12.3 ± 1.4 nm, respectively (Figure 5). This allowed to cover the 1.5–16 nm size regime, which is typically employed in most catalytic studies. The nanoparticles mostly have spherical shape, however octahedron type particles can also be observed in samples with larger nanoparticles.

To investigate the morphology of the Pt/NiO electrodes SEM and TEM images were recorded. SEM image of a Pt/NiO electrode (7.2 nm average Pt diameter) is compared to the corresponding bare NiO in Figure 6. Even at high magnifications, the 7.2 nm Pt nanoparticles are too small to be observed directly, however there are some distinguishable changes, which indicate the presence of Pt on the NiO surface. First, the surface is smoother before drop-casting of Pt, than afterward. Furthermore, upon drop-casting, the pore structure also altered: the diameter of the pores decreased and some were even clogged. The pore size distribution was also determined before and after decoration with Pt (Figure 6C). Most importantly, the fraction of the large pores decreased notably, due to the incorporation of Pt nanoparticles. The amount of the small pores increased in parallel as expected. These observations together indicate that a high amount of Pt nanoparticles accumulated in the pores, close to the top of the NiO layer.

TEM images of the debris of porous NiO films were scrutinized, and the presence of a mesoporous structure was witnessed. The average diameter of the joined building blocks were around 20 nm (Figure 7A). Note that this value is in perfect agreement with the previously shown XRD and SEM data. As for the Pt/NiO sample (containing 7.2 nm Pt), individual Pt nanoparticles can be spotted on the image (Figure 7B). The electron diffraction study of the nanoporous nickel oxide reveals NiO(111), Ni(200), NiO(200), NiO(220), NiO(311), and NiO(222) crystallite planes characteristic for face-centered cubic (*fcc*) nickel(II) oxide (Figure 7C). For Pt-decorated NiO, crystallite planes of Pt(111), Pt(200), and

DOI: 10.1021/acs.jpcc.7b00429
J. Phys. Chem. C 2017, 121, 12148–12158

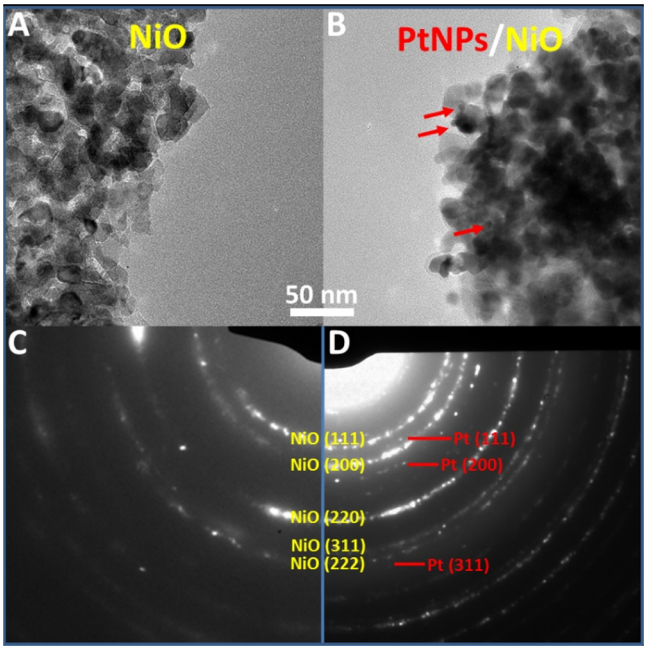

Figure 7. (A) Typical TEM images of a heat treated porous NiO and (B) a Pt/NiO sample containing 7.2 nm average diameter Pt nanoparticles with a surface concentration of 5 $\mu g/cm^2$. (C, D) Electron diffraction patterns of the respective materials shown in parts A and B.

Pt(311) showed the presence of metallic face-centered cubic (*fcc*) platinum (Figure 7D).

HR-TEM images were also recorded for a composite sample with higher Pt loading (10 $\mu g\ cm^{-2}$, Figure 8 and Figure S6).

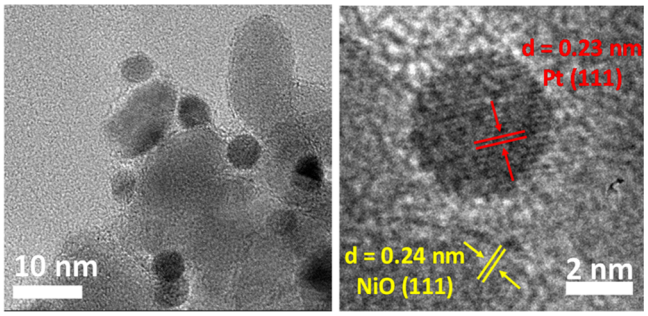

Figure 8. High-resolution TEM images of 7.2 nm Pt nanoparticles anchored onto the surface of nanoporous NiO.

The most important message of this TEM images is that nanosized Pt particles can be spotted anchored to the interconnected porous structure of NiO. In addition, clear lattice fringes corresponding to the (111) facets of Pt as well as the (111) facets of NiO were observed (Figure 8).

XPS Measurements. To evaluate the surface chemical characteristics of the NiO electrodes and the drop-casted Pt nanoparticles, XPS measurements were carried out. NiO-based materials exhibit complex surface chemistry because of nonstoichiometry and hydration under ambient conditions.[46] The presence of different Ni−oxide/hydroxide species can make the quantitative evaluation of the XP spectra problematic and should be only attempted in the presence of high quality standards.[46−48] In this vein, we focused on the qualitative evaluation of the surface characteristics. In Figure 9 regions corresponding to Ni 3p (A), Ni 2p (B), and O 1s (C) are shown for a NiO sample decorated with 8.6 nm average diameter Pt nanoparticles. Because of the extensive overlap between the Ni 3p and the Pt 4f signals, deconvolution of the Ni 3p components was not attempted. Judging from the position of the asymmetric Pt $4f_{7/2}$ component (71.2 eV), together with the Pt $4d_{5/2}$ peak positions (Figure S8) however, the zero valence of the drop-casted Pt can be confirmed in all cases (Figure 9A).[49,50] Notably, a small amount of surface oxide (PtO) was only detected in the case of the smallest Pt nanoparticles (Figure S8). The main Ni $2p_{3/2}$ line was modeled with three components: (i) NiO (853.7 eV) and (ii) $Ni(OH)_2$ (855.2 eV) and NiOOH (856.4 eV), which are consistent with literature data.[46] The addition of NiOOH into the model was dictated by the chemical nature of the samples, because its formation is characteristic of electrochemically grown NiO layers.[24,51] In the O 1s region (Figure 9C) similar chemical entities were distinguished in accordance with previous literature data.[46] When fitting the spectrum the contribution from oxygens of NiO (529.2 eV), $Ni(OH)_2$ (530.7 eV), NiOOH (532.1 eV), and physisorbed H_2O (532.9 eV) were all taken into account.

Electrochemical and Photoelectrochemical Characterization. To assess the dark electrochemical behavior of the Pt/NiO nanocomposites, cyclic voltammograms (CVs) were recorded (Figure 10A). Two main trends were immediately observed upon the addition of Pt: (i) a dark current developed in the range of $E = -1.0$ to -0.4 V (arising from direct water reduction on the Pt nanoparticles) and (ii) a change in the overall electroactivity of the electrodes. For pristine NiO, negligible dark current flow was observed at the cathodic end of the potential window ($E = -1.0$ to -0.4 V). When the surface

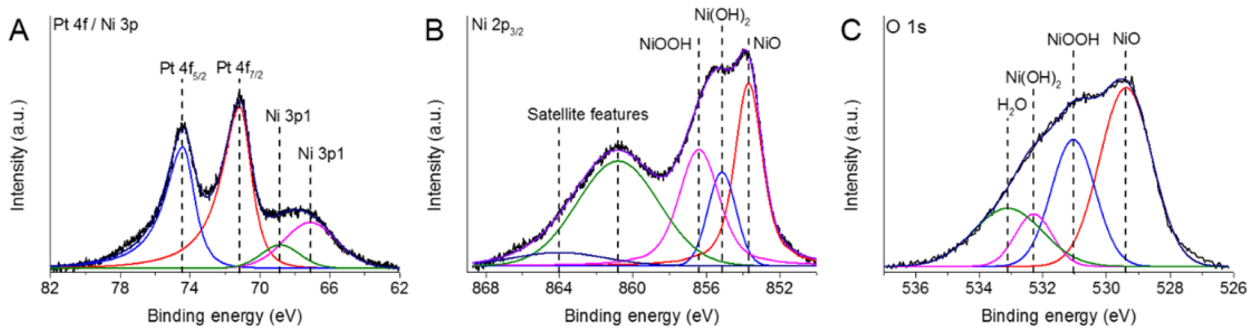

Figure 9. (A) Pt 4f/Ni 3p XP spectrum, (B) Ni $2p_{3/2}$ XP spectrum, and (C) and O 1s XP spectrum of the NiO sample decorated with 8.6 nm Pt nanoparticles. Resolved curves are added only to guide the eye to changes in spectral shape and do not represent sufficient component analysis.

DOI: 10.1021/acs.jpcc.7b00429
J. Phys. Chem. C 2017, 121, 12148−12158

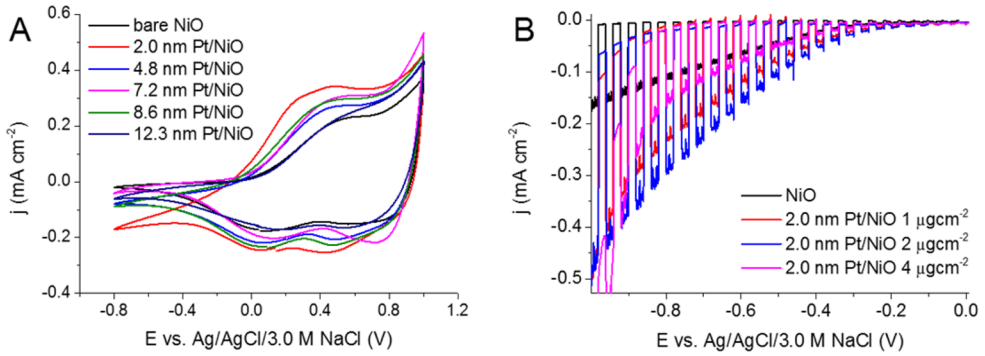

Figure 10. (A) Cyclic voltammograms of NiO and Pt/NiO composites 2 μg cm^{-2}. (B) Linear photovoltammogram of Pt/NiO 2.0 nm, with different Pt loading in 0.2 M Na_2SO_4, saturated with N_2 gas.

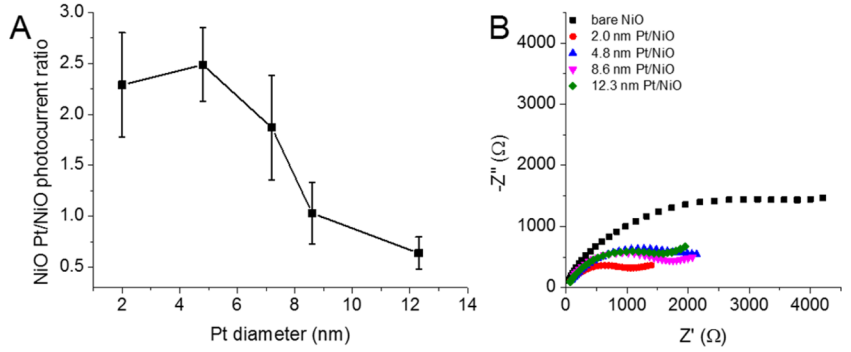

Figure 11. (A) Particle size dependence of the photocurrent enhancement for the Pt/NiO samples (2 μg cm^{-2} loading). The error bar represents measurements carried out for three different sample for each particle size. Lines connecting the measured data serve as guides for the eye only. (B) Nyquist plots of the electrochemical impedance spectroscopy data, recorded for the bare and different Pt-decorated NiO samples, at E = 0.0 V in the 10 Hz to 0.1 MHz frequency range, in 1.0 M Na_2SO_4 solution. The inset shows the magnified region of the semicircles.

of the NiO electrodes is decorated with Pt nanoparticles, however the gradual evolution of a dark current was witnessed. The onset potential of this process is located at E = −0.2 V regardless of the size of the Pt nanoparticles. This observation indicates that the size of the nanoparticles predominantly affects the kinetic aspects of the dark water reduction process. In the positive potential regime (E > 0.0 V) higher electrochemical activity was observed for the Pt loaded NiO samples compared to their pristine NiO counterpart. Although the electrochemical transformation of NiO and Pt overlap in this potential regime, the increased electroactivity can be attributed to the presence of Pt related redox peaks.[31,S2] Among all the studied samples the one decorated with 2.0 nm Pt nanoparticles exhibited the highest electrochemical activity, and the relative enhancement decreased with the increasing Pt particle size. These data served as the basis of normalization of the PEC performance (see below), where the actual surface area of the cocatalyst may play a key role in the overall performance.

To characterize the PEC behavior of the Pt/NiO composites, linear sweep photovoltammetry measurements were carried out with a slow sweep rate (2 mV s^{-1}) in 0.2 M Na_2SO_4. The illumination was periodically interrupted (0.1 Hz) to record the response of the electrodes under both dark and illuminated conditions. In almost all the cases (except for the largest Pt size), the cathodic photocurrents of the Pt-decorated NiO samples surpassed their pristine NiO counterparts. This superior behavior could be attributed to the more efficient electron−hole separation in the prepared nanocomposites.[23] By increasing the Pt loading, higher photocurrents were achieved until an optimal composition was reached. After this maximum, the optical shielding effect of the Pt nanoparticles on the surface resulted in a decrease in the photocurrents. For the largest particle, this shielding effect seemed to be deleterious even at moderate loadings. To strip the measured photocurrent enhancements from possible uncertainty arising from the use of different NiO electrodes, the photocurrents were normalized by the photocurrent measured for the respective pristine NiO electrodes (Figure S7). To find the optimal composition and particle size, these normalized photocurrent values were determined of each Pt decorated sample (Figure 11A, and Figure S7). It is apparent that the largest increase in the photocurrent value was achieved in the case of 2.0 and 4.8 nm sized Pt nanoparticles.

The origin of this photocurrent enhancement, however, is complex and convoluted. First of all, the surface area difference of the various sized Pt nanoparticles can be reflected in these increased values. To exclude this factor and to shed light on possible other, more sophisticated size-effects, further normalization of the data was carried out. The extra redox peak observed for the Pt-decorated samples during CV measurements is a direct indicator of the electroactive surface area of the Pt nanoparticles. As the first step, the charge capacitance of the bare NiO was subtracted from that of the Pt-decorated samples. Subsequently, the normalization of the photocurrent enhancement with respect of the electrochemically active surface area of the Pt nanoparticles was carried out. When the trivial surface area effect was stripped from the data the maximum photocurrent increase was obtained for the samples decorated with 4.8 and 7.2 nm sized Pt nanoparticles.

DOI: 10.1021/acs.jpcc.7b00429
J. Phys. Chem. C 2017, 121, 12148−12158

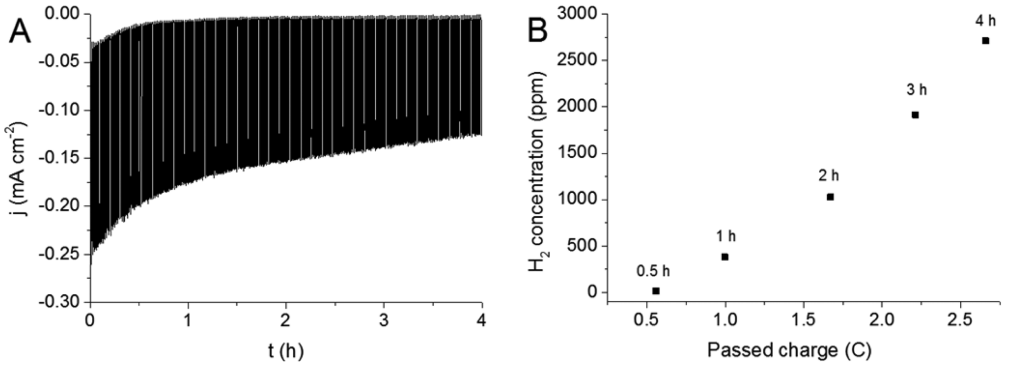

Figure 12. (A) Long-term photoelectrolysis on a Pt/NiO electrode (7.2 nm sized Pt) at $E = -0.8$ V potential in 0.2 M Na_2SO_4. (B) Amount of evolved H_2 during the long-term measurement shown in part A.

This observation is indeed interesting, because in earlier studies the highest heterogeneous/electrocatalytic activity was typically observed for even smaller particles (mostly because of the larger number of active sites).[30−35] In our case, however, the compatibility of the NiO and Pt has to be also considered. As the average pore size of the optimized NiO samples was 15 ± 5 nm (see also pore size distribution in Figure 1C), the large sized Pt particles simply do not infiltrate into the deeper regions of the nanoporous NiO film, but rather remain on its top. Such architecture is obviously not favorable considering the low contact area between NiO and Pt, and the possible optical shielding effect. On the other hand, the smallest (2 nm) Pt particles are likely to penetrate to the bottom region of the anodized NiO layer. As the light penetration is limited in the deeper regions, the cocatalytic effect of these deeply embedded Pt particles cannot be fully harnessed. Finally, the intermediate sized (4.8 and 7.2 nm) Pt particles may partially penetrate, resulting in a beneficial Pt/NiO nanoarchitectures. This hypothesis is qualitatively supported by XPS data, where the surface concentration of the Pt nanoparticles was estimated. It was found that the high specific surface area of the small sized Pt nanoparticles is not reflected in the surface Pt/Ni ratio, most likely because it is compensated by their increased penetration into the NiO layer (where they are invisible for XPS).

Electrochemical impedance spectroscopy (EIS) measurements were carried out to characterize the electrical properties of the Pt decorated NiO electrodes. The Nyquist-plots of the samples are presented in Figure 11B. Qualitatively, one may notice that the impedance spectra exhibit a depressed semicircle at high frequencies. It is also apparent that all Pt containing samples possess lower charge transfer resistance (the decrease in the end point of the semicircle) compared to the bare NiO electrodes. Overall, the lowest charge transfer resistance was obtained for the sample with the smallest Pt size, but all Pt-decorated electrodes have much smaller R_{ct}, compared to the bare NiO. This trend suggest that the photocurrent increase is rooted in the improved charge transfer at the electrode/electrolyte interface. Further details, including the fitting of EIS data and the employed equivalent circuit are shown in the Supporting Information (Figure S10 and Figure S11).

To further study the origin of the photocurrent enhancement, photoaction spectra were recorded. Figure S9 shows the photoaction spectra of the pristine and 2.0 nm sized Pt decorated NiO electrodes in 0.2 M Na_2SO_4 recorded at a constant bias potential of $E = -0.8$ V. The bandgap of the materials was estimated by fitting the cutoff region of the photoaction spectra with a straight line segment and extrapolating it to the wavelength axis. For both the pristine and Pt decorated samples a similar bandgap value of $E_{bg} = 3.55$ eV was found. This is in good agreement with the 3.5 eV value reported for NiO in the literature,[23] and our own optical data obtained via diffuse reflectance UV−vis spectroscopy (3.50 ± 0.1 eV, raw data not shown here). The decoration of the NiO electrodes with Pt nanoparticles leaves the bandgap of the oxide hybrids intact. Therefore, confirming our previous conclusion, the improvement in the PEC behavior of the Pt-decorated samples can be attributed to better charge separation rather than increased optical absorption.

Long-Term Photoelectrochemical Measurements. Long-term photoelectrolysis, combined with in situ gas phase analysis, was performed to monitor the formation of H_2 gas (Figure 12). At the initial stage of the photoelectrolysis some dark current was detected, most likely because of the reduction of some minority Ni(III) species in the sample (see also XPS data above). The measured photocurrents slowly decreased during the electrolysis, partly because of the leaching of Pt nanoparticles to the solution (as confirmed by comparing the XPS data before and after photoelectrolysis). After half an hour, there was a detectable amount of H_2 in the gas phase. The H_2 concentration increased linearly with the transferred charge. The Faradaic efficiency of this process was around 70%, most likely because of minor leaking of the electrochemical cell. Long-term measurements for other Pt/NiO electrodes (with different Pt sizes) were also conducted (not shown here), where a similar pattern was found. XPS investigations taken after the long-term measurements revealed that the chemical state of Pt and NiO was not altered during the process.

■ CONCLUSIONS

In this study, we carried out the simultaneous optimization of nanoporous NiO and Pt nanoparticles to assemble Pt/NiO composite photoelectrodes with improved PEC performance. This system served as a *model* for photoelectrodes encompassing a semiconductor light absorber and a metal nanoparticle cocatalyst. As the first step a new anodization protocol was developed, which allowed the formation of pure NiO, with controlled morphological attributes. In the second step, Pt nanoparticles were synthesized with precise size control (five sizes between 2.0 and 12.3 nm average diameter) and narrow size distribution. Finally, the Pt nanoparticles were anchored on the NiO surface with different loadings. All the hybrid samples showed enhanced cathodic photocurrents compared to the bare NiO film, although to notably different extents. It was shown that the enhanced PEC activity is rooted in the lower charge

DOI: 10.1021/acs.jpcc.7b00429
J. Phys. Chem. C 2017, 121, 12148−12158

carrier recombination rate in the case of the composite samples (i.e., Pt acted as a cocatalyst in the H_2 evolution reaction). Comparing the relative enhancements in the photocurrents upon the addition of different sized Pt particles, it was found that the two smallest (2.0 and 4.8 nm) have the most beneficial effect. After peeling off the trivial surface area effect (performed by normalizing the photocurrent enhancement with the electrochemically active surface area of Pt) the two intermediate particle sizes (4.8 and 7.2 nm) were found to be significantly better than both the smaller and larger particles. The main outcome of this study is that the size of the cocatalyst exerts an important role in the overall performance, similarly to the electrocatalytic and photocatalytic scenarios.[30−35] The complete picture, however, is even more complicated because light absorption, charge carrier transport, and surface chemical reactions have to be considered at the same time. We have demonstrated that in the case of nanocomposite photoelectrodes (e.g., light absorber + cocatalyst) the nanoscale structure of the components has to be optimized simultaneously, to achieve reasonable PEC activity. The conclusions of this study may lead to new design concepts of photoelectrode assemblies, and such endeavors are in progress in our laboratories.

■ ASSOCIATED CONTENT

Supporting Information

The Supporting Information is available free of charge on the ACS Publications website at DOI: 10.1021/acs.jpcc.7b00429.

Additional SEM images, EDX spectra, description of Pt nanoparticle synthesis, TEM images, PEC data, XP spectra, photoaction spectra, and electrochemical impedance spectra (PDF)

■ AUTHOR INFORMATION

Corresponding Author

*(C.J.) E-mail: janaky@chem.u-szeged.hu.

ORCID

András Sápi: 0000-0001-6557-0731

Csaba Janáky: 0000-0001-5965-5173

Notes

The authors declare no competing financial interest.

■ ACKNOWLEDGMENTS

The authors thank Dr. Tamás Pajkossy (Research Center for Natural Sciences of the Hungarian Academy of Sciences) for the valuable discussions on the EIS results. The authors are very thankful to Prof. Frank Osterloh (University of California, Davis) for his constructive criticism and insightful comments on an earlier version of this manuscript. The authors are grateful for Ildikó Kálomista and Prof. Gábor Galbács for ICP-MS measurements. The authors acknowledge the assistance of the colleagues at Rendernet Ltd., provided in the preparation of the artwork. This project has received funding from the European Research Council (ERC) under the European Union's Horizon 2020 research and innovation programme (Grant Agreement No 716539). This collaborative research was partially supported by the "Széchenyi 2020" program in the framework of GINOP-2.3.2-15-2016-00013 "Intelligent materials based on functional surfaces−from syntheses to applications" project and the Hungarian National Research Development and Innovation Office through projects K K 112531, K 120115, and PD 120877. This paper was also supported by the János Bolyai Research Scholarship of the Hungarian Academy of Sciences and the ÚNKP-ÚNKP-16-4 New National Excellence Program of the Ministry of Human Capacities (A. S.).

■ REFERENCES

(1) Lewis, N.; Nocera, D. Powering the Planet: Chemical Challenges in Solar Energy Utilization. *Proc. Natl. Acad. Sci. U. S. A.* **2006**, *103*, 15729−15735.

(2) Lewis, N. S. Research Opportunities to Advance Solar Energy Utilization. *Science* **2016**, *351*, 353−362.

(3) Chen, Z.; Jaramillo, T. F.; Deutsch, T. G.; Kleiman-Shwarsctein, A.; Forman, A. J.; Gaillard, N.; Garland, R.; Takanabe, K.; Heske, C.; Sunkara, M.; et al. Accelerating Materials Development for Photoelectrochemical Hydrogen Production: Standards for Methods, Definitions, and Reporting Protocols. *J. Mater. Res.* **2010**, *25*, 3−16.

(4) Rajeshwar, K. Hydrogen Generation at Irradiated Oxide Semiconductor−solution Interfaces. *J. Appl. Electrochem.* **2007**, *37*, 765−787.

(5) Rajeshwar, K. Solar Energy Conversion and Environmental Remediation Using Inorganic Semiconductor−Liquid Interfaces: The Road Traveled and the Way Forward. *J. Phys. Chem. Lett.* **2011**, *2*, 1301−1309.

(6) van de Krol, R. Principles of Photoelectrochemical Cells. In *Photoelectrochemical Hydrogen Production*; van de Krol, R., Gratzel, M., Eds.; Springer: 2012; Vol. *102*, pp 13−67.

(7) Khaselev, O.; Turner, J. A. A Monolithic Photovoltaic-Photoelectrochemical Device for Hydrogen Production via Water Splitting. *Science* **1998**, *280*, 425−427.

(8) Sun, K.; Liu, R.; Chen, Y.; Verlage, E.; Lewis, N. S.; Xiang, C. A Stabilized, Intrinsically Safe, 10% Efficient, Solar-Driven Water-Splitting Cell Incorporating Earth-Abundant Electrocatalysts with Steady-State pH Gradients and Product Separation Enabled by a Bipolar Membrane. *Adv. Energy Mater.* **2016**, *6*, 1600379.

(9) Kamat, P. V.; Christians, J. A. Solar Cells versus Solar Fuels: Two Different Outcomes. *J. Phys. Chem. Lett.* **2015**, *6*, 1917−1918.

(10) Osterloh, F. E. Inorganic Nanostructures for Photoelectrochemical and Photocatalytic Water Splitting. *Chem. Soc. Rev.* **2013**, *42*, 2294−2320.

(11) Sivula, K.; van de Krol, R. Semiconducting Materials for Photoelectrochemical Energy Conversion. *Nat. Rev. Mater.* **2016**, *1*, 15010.

(12) Bang, J. H.; Kamat, P. V. Solar Cells by Design: Photoelectrochemistry of TiO_2 Nanorod Arrays Decorated with CdSe. *Adv. Funct. Mater.* **2010**, *20*, 1970−1976.

(13) Liu, N.; Lee, K.; Schmuki, P. Small Diameter TiO_2 Nanotubes vs. Nanopores in Dye Sensitized Solar Cells. *Electrochem. Commun.* **2012**, *15*, 1−4.

(14) Janáky, C.; Chanmanee, W.; Rajeshwar, K. On the Substantially Improved Photoelectrochemical Properties of Nanoporous WO_3 Through Surface Decoration with RuO_2. *Electrocatalysis* **2013**, *4*, 382−389.

(15) Bignozzi, C. A.; Caramori, S.; Cristino, V.; Argazzi, R.; Meda, L.; Tacca, A. Nanostructured Photoelectrodes Based on WO_3: Applications to Photooxidation of Aqueous Electrolytes. *Chem. Soc. Rev.* **2013**, *42*, 2228−2246.

(16) Hu, L.; Peng, J.; Wang, W.; Xia, Z.; Yuan, J.; Lu, J.; Huang, X.; Ma, W.; Song, H.; Chen, W.; et al. Sequential Deposition of $CH_3NH_3PbI_3$ on Planar NiO Film for Efficient Planar Perovskite Solar Cells. *ACS Photonics* **2014**, *1*, 547−553.

(17) Nattestad, A.; Mozer, A. J.; Fischer, M. K. R.; Cheng, Y.; Mishra, A.; Bäuerle, P.; Bach, U. Efficient Photocathodes for Dye-Sensitized Tandem Solar Cells. *Nat. Mater.* **2010**, *9*, 31−35.

(18) Li, L.; Gibson, E. A.; Qin, P.; Boschloo, G.; Gorlov, M.; Hagfeldt, A.; Sun, L. Double-Layered NiO Photocathodes for P-Type DSSCs with Record IPCE. *Adv. Mater.* **2010**, *22*, 1759−1762.

DOI: 10.1021/acs.jpcc.7b00429
J. Phys. Chem. C 2017, 121, 12148−12158

(19) Dare-edwards, M. P.; Goodenough, J.; Hamnett, A.; Nicholson, N. D. Photoelectrochemistry of Nickel (II) Oxide. *J. Chem. Soc., Faraday Trans. 2* **1981**, *77*, 643−661.
(20) Lin, C.-Y.; Lai, Y.-H.; Mersch, D.; Reisner, E. $Cu_2O|NiO_x$ Nanocomposite as an Inexpensive Photocathode in Photoelectrochemical Water Splitting. *Chem. Sci.* **2012**, *3*, 3482.
(21) Gross, M. A.; Creissen, C. E.; Orchard, K. L.; Reisner, E. Photoelectrochemical Hydrogen Production in Water Using a Layer-by-Layer Assembly of a Ru Dye and Ni Catalyst on NiO. *Chem. Sci.* **2016**, *7*, 5537−5546.
(22) Sahara, G.; Abe, R.; Higashi, M.; Morikawa, T.; Maeda, K.; Ueda, Y.; Ishitani, O. Photoelectrochemical CO_2 Reduction Using a Ru(II)-Re(I) Multinuclear Metal Complex on a P-Type Semiconducting NiO Electrode. *Chem. Commun.* **2015**, *51*, 10722−10725.
(23) Nail, B. A.; Fields, J. M.; Zhao, J.; Wang, J.; Greaney, M. J.; Brutchey, R. L.; Osterloh, F. E. Nickel Oxide Particles Catalyze Photochemical Hydrogen Evolution from Water—Nanoscaling Promotes P-Type Character and Minority Carrier Extraction. *ACS Nano* **2015**, *9*, 5135−5142.
(24) Hu, C.; Chu, K.; Zhao, Y.; Teoh, W. Y. Efficient Photoelectrochemical Water Splitting over Anodized P -Type NiO Porous Films. *ACS Appl. Mater. Interfaces* **2014**, *6*, 18558−18568.
(25) Sun, K.; McDowell, M. T.; Nielander, A. C.; Hu, S.; Shaner, M. R.; Yang, F.; Brunschwig, B. S.; Lewis, N. S. Stable Solar-Driven Water Oxidation to $O_2(g)$ by Ni-Oxide-Coated Silicon Photoanodes. *J. Phys. Chem. Lett.* **2015**, *6*, 592−598.
(26) Kenney, M. J.; Gong, M.; Li, Y.; Wu, J. Z.; Feng, J.; Lanza, M.; Dai, H. High-Performance Silicon Photoanodes Passivated with Ultrathin Nickel Films for Water Oxidation. *Science* **2013**, *342*, 836−840.
(27) Subramanian, V.; Wolf, E. E.; Kamat, P. V. Catalysis with TiO_2 /Gold Nanocomposites. Effect of Metal Particle Size on the Fermi Level Equilibration. *J. Am. Chem. Soc.* **2004**, *126*, 4943−4950.
(28) Subramanian, V.; Wolf, E.; Kamat, P. V. Semiconductor - Metal Composite Nanostructures. To What Extent Do Metal Nanoparticles Improve the Photocatalytic Activity of TiO_2 Films? *J. Phys. Chem. B* **2001**, *105*, 11439−11446.
(29) McCrory, C. C. L.; Jung, S.; Ferrer, I. M.; Chatman, S. M.; Peters, J. C.; Jaramillo, T. F. Benchmarking Hydrogen Evolving Reaction and Oxygen Evolving Reaction Electrocatalysts for Solar Water Splitting Devices. *J. Am. Chem. Soc.* **2015**, *137*, 4347−4357.
(30) Shao, M.; Peles, A.; Shoemaker, K. Electrocatalysis on Platinum Nanoparticles: Particle Size Effect on Oxygen Reduction Reaction Activity. *Nano Lett.* **2011**, *11*, 3714−3719.
(31) Arenz, M.; Mayrhofer, K. J. J.; Stamenkovic, V.; Blizanac, B. B.; Tomoyuki, T.; Ross, P. N.; Markovic, N. M. The Effect of the Particle Size on the Kinetics of CO Electrooxidation on High Surface Area Pt Catalysts. *J. Am. Chem. Soc.* **2005**, *127*, 6819−6829.
(32) Sapi, A.; Liu, F.; Cai, X.; Thompson, C. M.; Wang, H.; An, K.; Krier, J. M.; Somorjai, G. A. Comparing the Catalytic Oxidation of Ethanol at the Solid−Gas and Solid−Liquid Interfaces over Size-Controlled Pt Nanoparticles: Striking Differences in Kinetics and Mechanism. *Nano Lett.* **2014**, *14*, 6727−6730.
(33) Wang, H.; Wang, Y.; Zhu, Z.; Sapi, A.; An, K.; Kennedy, G.; Michalak, W. D.; Somorjai, G. A. Influence of Size-Induced Oxidation State of Platinum Nanoparticles on Selectivity and Activity in Catalytic Methanol Oxidation in the Gas Phase. *Nano Lett.* **2013**, *13*, 2976−2979.
(34) Wang, H.; Sapi, A.; Thompson, C. M.; Liu, F.; Zherebetskyy, D.; Krier, J. M.; Carl, L. M.; Cai, X.; Wang, L.-W.; Somorjai, G. A. Dramatically Different Kinetics and Mechanism at Solid/Liquid and Solid/Gas Interfaces for Catalytic Isopropanol Oxidation over Size-Controlled Platinum Nanoparticles. *J. Am. Chem. Soc.* **2014**, *136*, 10515−10520.
(35) Pushkarev, V. V.; An, K.; Alayoglu, S.; Beaumont, S. K.; Somorjai, G. A. Hydrogenation of Benzene and Toluene over Size Controlled Pt/SBA-15 Catalysts: Elucidation of the Pt Particle Size Effect on Reaction Kinetics. *J. Catal.* **2012**, *292*, 64−72.
(36) Kmetykó, Á.; Mogyorósi, K.; Gerse, V.; Kónya, Z.; Pusztai, P.; Dombi, A.; Hernádi, K. Photocatalytic H_2 Production Using Pt-TiO_2 in the Presence of Oxalic Acid: Influence of the Noble Metal Size and the Carrier Gas Flow Rate. *Materials* **2014**, *7*, 7022−7038.
(37) Wang, W.; An, W.; Ramalingam, B.; Mukherjee, S.; Niedzwiedzki, D. M.; Gangopadhyay, S.; Biswas, P. Size and Structure Matter: Enhanced CO_2 Photoreduction Efficiency by Size-Resolved Ultrafine Pt Nanoparticles on TiO_2 Single Crystals. *J. Am. Chem. Soc.* **2012**, *134*, 11276−11281.
(38) Lombardi, I.; Marchionna, S.; Zangari, G.; Pizzini, S. Effect of Pt Particle Size and Distribution on Photoelectrochemical Hydrogen Evolution by P-Si Photocathodes. *Langmuir* **2007**, *23*, 12413−12420.
(39) Shrestha, N. K.; Yang, M.; Schmuki, P. Self-Ordered Nanoporous Nickel Oxide/Fluoride Composite Film with Strong Electrochromic Contrast. *Electrochem. Solid-State Lett.* **2010**, *13*, C21−C24.
(40) Roy, P.; Berger, S.; Schmuki, P. TiO_2 Nanotubes: Synthesis and Applications. *Angew. Chem., Int. Ed.* **2011**, *50*, 2904−2939.
(41) Samu, G. F.; Pencz, K.; Janáky, C.; Rajeshwar, K. On the Electrochemical Synthesis and Charge Storage Properties of WO_3/polyaniline Hybrid Nanostructures. *J. Solid State Electrochem.* **2015**, *19*, 2741−2751.
(42) Macak, J. M.; Hildebrand, H.; Marten-Jahns, U.; Schmuki, P. Mechanistic Aspects and Growth of Large Diameter Self-Organized TiO_2 Nanotubes. *J. Electroanal. Chem.* **2008**, *621*, 254−266.
(43) Zhou, G.; Wang, D.-W.; Yin, L.-C.; Li, N.; Li, F.; Cheng, H.-M. Oxygen Bridges between NiO Nanosheets and Graphene for Improvement of Lithium Storage. *ACS Nano* **2012**, *6*, 3214−3223.
(44) Marrani, A. G.; Novelli, V.; Sheehan, S.; Dowling, D. P.; Dini, D. Probing the Redox States at the Surface of Electroactive Nanoporous NiO Thin Films. *ACS Appl. Mater. Interfaces* **2014**, *6*, 143−152.
(45) Bode, H.; Dehmelt, K.; Witte, J. Zur Kenntnis Der nickelhydroxidelektrode-I.Über Das Nickel (II)-Hydroxidhydrat. *Electrochim. Acta* **1966**, *11*, 1079−IN1.
(46) Ratcliff, E. L.; Meyer, J.; Steirer, K. X.; Garcia, A.; Berry, J. J.; Ginley, D. S.; Olson, D. C.; Kahn, A.; Armstrong, N. R. Evidence for near-Surface NiOOH Species in Solution-Processed NiO_x Selective Interlayer Materials: Impact on Energetics and the Performance of Polymer Bulk Heterojunction Photovoltaics. *Chem. Mater.* **2011**, *23*, 4988−5000.
(47) Biesinger, M. C.; Payne, B. P.; Lau, L. W. M.; Gerson, A.; Smart, R. S. C. X-Ray Photoelectron Spectroscopic Chemical State Quantification of Mixed Nickel Metal, Oxide and Hydroxide Systems. *Surf. Interface Anal.* **2009**, *41*, 324−332.
(48) Biesinger, M. C.; Payne, B. P.; Grosvenor, A. P.; Lau, L. W. M.; Gerson, A. R.; Smart, R. S. C. Resolving Surface Chemical States in XPS Analysis of First Row Transition Metals, Oxides and Hydroxides: Cr, Mn, Fe, Co and Ni. *Appl. Surf. Sci.* **2011**, *257*, 2717−2730.
(49) Sun, Y.; Wang, Y.; Pan, J. S.; Wang, L.; Sun, C. Q. Elucidating the 4f Binding Energy of an Isolated Pt Atom and Its Bulk Shift from the Measured Surface- and Size-Induced Pt 4f Core Level Shift. *J. Phys. Chem. C* **2009**, *113*, 14696−14701.
(50) Shyu, J. Z.; Otto, K. Identification of Platinum Phases on γ-Alumina by XPS. *Appl. Surf. Sci.* **1988**, *32*, 246−252.
(51) Beverskog, B.; Puigdomenech, I. Revised Pourbaix Diagrams for Nickel at 25−300 °C. *Corros. Sci.* **1997**, *39*, 969−980.
(52) Mayrhofer, K. J. J.; Blizanac, B. B.; Arenz, M.; Stamenkovic, V. R.; Ross, P. N.; Markovic, N. M. The Impact of Geometric and Surface Electronic Properties of Pt-Catalysts on the Particle Size Effect in Electrocatalysis. *J. Phys. Chem. B* **2005**, *109*, 14433−14440.

DOI: 10.1021/acs.jpcc.7b00429
J. Phys. Chem. C 2017, 121, 12148−12158